Available online at https://link.springer.com/journal/42241
http://www.jhydrodynamics.com
Journal of Hydrodynamics, 2020, 32(2): 345-360
https://doi.org/10.1007/s42241-019-0034-0

Large eddy simulation of the transient cavitating vortical flow in a jet pump with special emphasis on the unstable limited operation stage*

Xin-ping Long[1, 2, 3], Dan Zuo[1, 2, 3], Huai-yu Cheng[1, 2, 3], Bin Ji[3]
1. *Hubei Key Laboratory of Waterjet Theory and New Technology, School of Power and Mechanical Engineering, Wuhan University, Wuhan 430072, China*
2. *Key Laboratory of Transients in Hydraulic Machinery, Ministry of Education, Wuhan University, Wuhan 430072, China*
3. *State Key Laboratory of Water Resources and Hydropower Engineering Science, Wuhan University, Wuhan 430072, China*

(Received November 9, 2018, Revised February 26, 2019, Accepted March 28, 2019, Published online April 12, 2019)

Abstract: This paper studies the unsteady three-dimensional cavitating turbulent flow in a jet pump. Specifically, thefocus is on the unstable limited operation stage, and both the computational and experimental methods are used. In the experiments, the distribution of the wall pressure, as well as the evolution of cavitation over time, are obtained for a jet pump. Computation is carried out using the large eddy simulation, combined with a mass transfer cavitation model. The numerical results are compared with the experimental results, including the fundamental performances (the pressure ratio h and the efficiency η), as well as the wall pressure distribution. Both the experimental and computational results indicate that the evolution of the cavitation over time in a jet pump is a quasi-periodic process during the unstable limited operation stage. The annular vortex cavitation inception, development and collapse predicted by the large eddy simulation agree fairly well with the experimental observations. Furthermore, the relationship between the cavitation and the vortex structure is discussed based on the numerical results, and it is shown that the development of the vortex structures in the jet pump is closely related to the evolution of the cavitation. The cavitation-vortex interaction is thoroughly analyzed based on the vorticity transport equation. This analysis reveals that the cavitation in a jet pump dramatically influences the distribution and the production of the vorticity. The process of the annular cavitation inception, development, and collapse involves a significant increase of the vorticity.

Key words: Cavitation, jet pump, large eddy simulation, vortex structure, vorticity transport equation

Introduction

A jet pump is a type of pumps that works by transferring the energy, the mass, and the heat from a high velocity primary flow to a secondary flow[1]. Due to the absence of rotating parts, their easy manufacturing, the reliable operation, and the easy installation and maintenance, the jet pumps are widely used in various engineering fields[2-3]. As fluid machineries, using the liquid as a working medium, the cavitation occurs in the jet pumps. The cavitation is a phase transition from the liquid to the vapor that occurs within a liquid or at the liquid-solid interface because of the power of the liquid's flow. Usually, the cavitation induced in a jet pump leads to noise and vibration, surface erosion, and reduced performance[4]. However, the cavitation effects such as the high pressure pulsation, the high temperature, and the strong oxide can also produce unexpected benefits when the cavitation bubbles collapse in a specified location[5]. Unlike the cavitation in a traditional centrifugal pump, the cavitation in a jet pump is as hear cavitation[6]. Thus, the cavitation in a jet pump is closely related to the vortex flow structure, and this important relation must be studied. All in all, the cavitation in a jet pump should be studied, both in the utilization and prevention views.

The cavitation performance of the jet pump was widely studied. Experimental studies are an important part. Long et al.[7] found that the critical liquid-vapor

---

* Project supported by the National Natural Science Foundation of China (Grant Nos. 51679169, 11472197).
Biography: Xin-ping Long (1956-), Male, Ph. D., Professor
Corresponding author: Xin-ping Long,
E-mail: xplong@whu.edu.cn

two-phase flow occurred when a jet pump worked under the operating limit. During the process of decreasing the cavitation number, the cavitation can be divided into four stages generally, as the incipient cavitation, the sheet cavitation, the cloud cavitation and the super cavitation. Similarly, the cavitation in jet pumps can also be divided into four stages: the inception stage, the developing stage, and the limited operation stage, with the limited operation stage being further divided into the unstable limited operation stage and the stable limited operation stage, according to the oscillation property of the cavitation cloud in the throat. In the unstable limited operation stage, the cavitation bubbles are induced constantly in the annular vortex structure, and then they gather together to form a cavity cloud, which grows and shrinks along the throat. Furthermore, the cavity cloud chokes the throat and pulsates violently until a severe collapse, producing much noise and vibration. So, the cavitation flow in the unstable limited operation stage is important for both controlling and using the cavitation. In addition, the studies of the cavitation in jet pumps also concern with other aspects. Xiao and Long[8] studied the instantaneous pulsation characteristics of a cavitation cloud in an annular jet pump. Long et al.[4] investigated the flow characteristics of a jet pump for flow ratios varying from the maximum to -1. The results indicate that the pressure ratio has a crucial effect on the change of the cavitation area in the negative flow ratios.

Experimental analyses assessing the cavitation can supply information about the incubation time and the position, but cannot reveal all aspects of the underlying flow dynamics. Therefore, numerical simulations of the cavitating flows is an important tool in the design process[9-11]. Both the cavitation model and the turbulence model play a significant role in the simulation of the cavitating flow. The widely used cavitation models can be divided into two categories. In the barotropic equation models (BEM), a barotropic state law is used to link the fluid density with the pressure variations, and these models have obvious defects in describing the phase transition process and predicting the convection and cavitation transport phenomena. In the transport equation-based models (TEM), the density fields are determined by the transport equation. Various comparative studies of these cavitation models are found in literature[12-13]. The Zwart TEM cavitation model is one that is widely used. With this model, the cavitation flows around the hydrofoil, the guide vane, and the venturi tube are evaluated with the flow details being well captured. The Zwart cavitation model is used in this paper, because of its success in capturing the features of the cavitation flows.

As for the turbulence modeling, early studies of submerged injection nozzles were based on solving the incompressible Reynolds-averaged Navier-Stokes (RANS) equations. Zhu and Rodi[14] computed the confined coflow jets with three turbulence models. Their results show that the realizable k - ε model can capture more flow characteristics than the standard k - ε model. Xiao and Long[8] used the realizable k - ε turbulence model, which could accurately predict the traditional jet pump performance but fail to capture the cavitation generation at the shearing layer. RANS approaches with eddy viscosity turbulence models have a limited capability to capture the unsteadiness of the cavitating flows, with over-predictions of the turbulent eddy viscosity.

Duke et al.[15] suggested using the large eddy simulation (LES) to capture the large turbulent features and the cavitation features in the nozzle flow. With the LES of the cavitating flows, some promising results were obtained for predicting larger-scale turbulent eddies. Dittakavi et al.[16] applied the LES in a venturi nozzle and observed that the formation of a vapor in the throat region suppresses the turbulent velocity fluctuations. Ji et al.[17] numerically investigated the complex cavitating flows around a NACA66 hydrofoil. The cavity shedding was theoretically related to the pressure fluctuations by a simplified one dimensional model. Long et al.[18] developed a three dimensional Lagrangian technology for the cavitating flow to study the behaviors of the re-entrant and side-entrant jets based both on the Euler and Lagrangian formulations.

Although the LES has achieved remarkable results in many aspects, related studies for the jet pumps were few. Xu et al.[19] studied the coherent structure of the turbulent flow in annular jet pumps with different area ratios based on the LES and revealed various characteristics of the coherent structure with different criteria. Zi et al.[20] analyzed the jet pump cavitation using the LES and found the pressure field in the shearing layer was dependent on both the overall mean pressure and the local shear strain rate, for the jet pump to produce different cavitation shapes. However, these studies did not pay much attention to the complicated flow structure in a jet pump or to the possibility of using the LES to accurately simulate a jet pump's cavitating flow.

The present work uses the LES combined with the experimental analysis to investigate the unstable limited operation stage of a jet pump. The evolution of the annular vortex cavitation's inception, developing, and collapsing is investigated. The formation mechanism of the cavitation in a jet pump from the vortex formation process is shown. Finally, the present work analyzes the interactions between the cavitation and the vortex in a jet pump based on the vorticity transport equation.

1. Experimental setup

Figure 1 shows the design of the tested jet pump, as is described in the previous paper[21]. The jet pump has five parts: the inlet pipe, the nozzle, the suction chamber, the throat, and the diffuser. While the nozzle is made of brass, the other parts of the jet pump are made of organic glass for the convenience of observation. The high pressure primary flow runs through the nozzle exit at a very high speed with an entrainment effect on the low pressure secondary flow in the suction chamber. The two flows mix intensively in the throat and then flow out through the diffuser with a pressure recovery. In the following, the throat entrance plane is set as the origin of an underlying Cartesian coordinate system.

Table 1 summarizes the main dimensions of the jet pump. The diameter of the nozzle exit D_n is 12 mm, and the diameter of the throat D_{th} is 16 mm, which corresponds to an area ratio of 1.78.

Figure 2 shows the experimental setup. The high pressure driving the primary flow (Q_{in}) supplied by a centrifugal pump entrains the secondary flow (Q_s) from the water tank. Then the mixed flow (Q_{out}) exchanges the momentum and the energy in the throat and the diffuser before flowing back to the water tank. The flow rates of the primary flow and the mixed flow are controlled by valves and measured by electro-

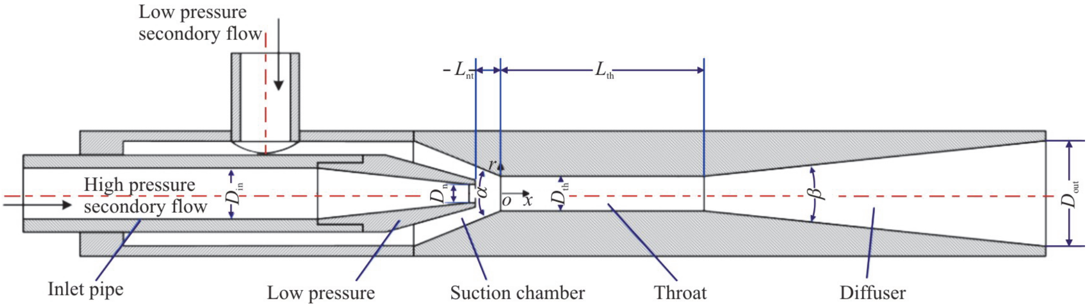

Fig. 1 (Color online) Schematic drawing of jet pump

Table 1 Main structural parameters of jet pump

D_{in} /mm	D_n /mm	D_{th} /mm	D_{out} /mm	L_{nt} /mm	L_{th} /mm	α /°	β /°
25	12	16	50	13	96	45	12

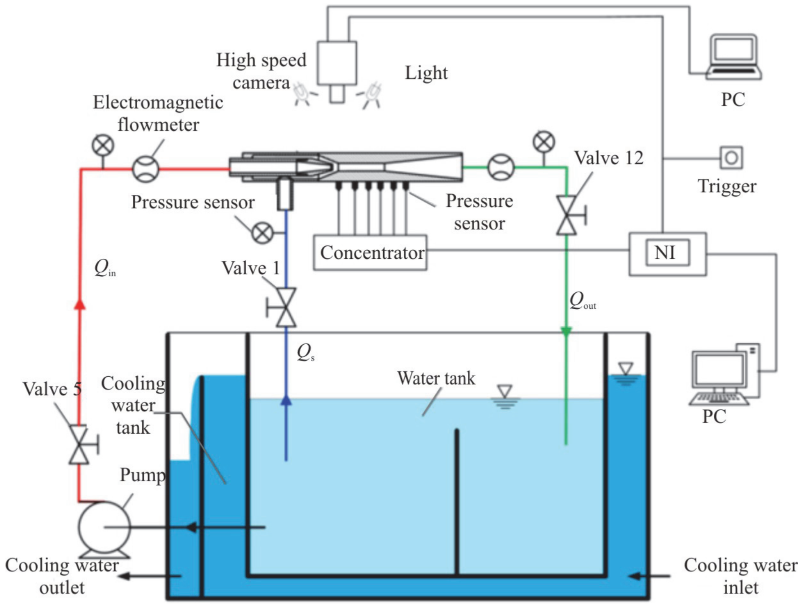

Fig. 2 (Color online) Sketch of the experimental rig

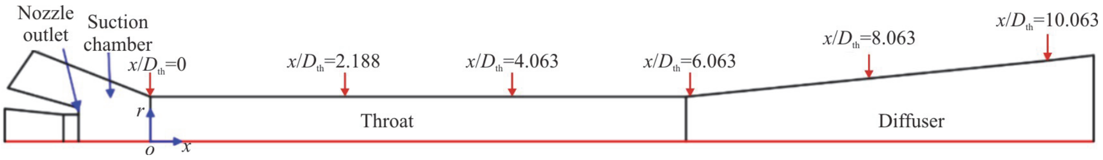

Fig. 3 (Color online) The installation position of high frequency pressure sensor

Table 2 Main structural parameters of jet pump

Camera type	Lenses type	Power of the lights	Minimum focus length	Frame rate
Photron FASTCAM SA5 8G	AF-S 105 mm f/2.8G	120 W	0.31 m	20 000 fps

magnetic flow-meters (KORHNE ISF4000) with an accuracy of 0.3%. Three pressure transducers (CHAOYU CY3011) are installed at the inlet pipes, the suction pipe, and the outlet pipe. These normal transducers are used to measure the hydrodynamic performance of the jet pump. Another six high frequency pressure transducers (HELM HM91) with a sampling rate of 100 kHz are installed along the throat and the diffuser to monitor the wall pressure distribution where there will be the fluctant pressures under the cavitation conditions. The installation position is shown in Fig. 3. The accuracy of the pressure sensors at the full scale is 0.5%. The whole system is a closed-loop system, and the cooling water tank is added to control the water temperature. The collected flow rate and pressure (absolute pressure) are recorded by a personal computer via NI PXI 6238 and 6143 data acquisition cards. The cavitation images of the flow in the unstable limited operation stage are captured by a high-speed camera of model Photron FASTCAM SA5, with a frame rate of 20 000 fps. Table 2 shows the main parameters of the high speed camera system.

The water level in the water tank is adjusted to a stable level before the tests. The air in the system is then expelled. After the preparatory work, the inlet pressure is adjusted to the desired value by adjusting the inlet valve 2. The outlet pressure is controlled by the valve 11. Once the flow parameter is adjusted to the designated value and held steady, the experimental data is collected. The images of the cavitating flow are captured by the high speed camera at the same time. The water temperature is kept around 25°C by the cooling water tank.

2. Mathematical formulations and numerical methods

2.1 *Cavitation model*

The cavitation model used in this study was developed by Zwart et al.[22], and its accuracy was widely validated. The cavitation process is governed by the mass transfer equation

$$\frac{\partial(\rho_{\mathrm{v}}\alpha_{\mathrm{v}})}{\partial t}+\frac{\partial(\rho_{\mathrm{v}}\alpha_{\mathrm{v}}u_{\mathrm{j}})}{\partial x_{\mathrm{j}}}=m^{+}-m^{-} \tag{1}$$

where m^{+} and m^{-} are the mass transfer rates for the vaporization and condensation processes, respectively. The simplified Rayleigh-Plesset equation, neglecting the second order derivative of the bubble radius[22] and the surface tension, can be written as

$$\frac{3}{2}\left(\frac{\mathrm{d}R_{\mathrm{B}}}{\mathrm{d}t}\right)^{2}=\frac{p_{\mathrm{v}}-p}{\rho_{\mathrm{l}}} \tag{2}$$

The growth rate can be related to the fluid pressure during the vaporization as

$$\frac{\mathrm{d}R_{\mathrm{B}}}{\mathrm{d}t}=\sqrt{\frac{2}{3}\frac{|p_{\mathrm{v}}-p|}{\rho_{\mathrm{l}}}} \tag{3}$$

where R_{B} is the bubble diameter, p_{v} is the saturated vapor pressure. The rate of change of the bubble mass can be written as

$$\frac{\mathrm{d}m_{\mathrm{B}}}{\mathrm{d}t}=\rho_{\mathrm{v}}\frac{\mathrm{d}V_{\mathrm{B}}}{\mathrm{d}t}=\rho_{\mathrm{v}}\frac{\mathrm{d}}{\mathrm{d}t}\left(\frac{4}{3}\pi R_{\mathrm{B}}^{3}\right)=4\pi\rho_{\mathrm{v}}R_{\mathrm{B}}^{2}\sqrt{\frac{2}{3}\frac{|p_{\mathrm{v}}-p|}{\rho_{\mathrm{l}}}} \tag{4}$$

where V_{B} is the bubble volume. Assuming that there are N_{B} bubbles per unit volume, the vapor volume fraction α_{v} can be expressed as

$$\alpha_{\mathrm{v}}=V_{\mathrm{B}}N_{\mathrm{B}}=\frac{4}{3}\pi R_{\mathrm{B}}^{3}N_{\mathrm{B}} \tag{5}$$

Then, the total mass transfer rate per unit volume is expressed as

$$m^{+} = N_{\mathrm{B}} \frac{\mathrm{d}m_{\mathrm{B}}}{\mathrm{d}t} = \frac{3\alpha_{\mathrm{v}}\rho_{\mathrm{v}}}{R_{\mathrm{B}}} \sqrt{\frac{2}{3} \frac{|p_{\mathrm{v}} - p|}{\rho_{\mathrm{l}}}} \tag{6}$$

This expression is derived for the vaporization process, and it can be generalized to include the condensation as follows

$$m^{-} = C_{\mathrm{cond}} \frac{3\alpha_{\mathrm{v}}\rho_{\mathrm{v}}}{R_{\mathrm{B}}} \sqrt{\frac{2}{3} \frac{\max(p - p_{\mathrm{v}}, 0)}{\rho_{\mathrm{l}}}} \tag{7}$$

where C_{cond} is an empirical constant for the condensation and set as 0.01. The bubble radius R_{B} is set to a constant 10^{-6}m. For the vaporization, the nucleation site density decreases when the vapor volume fraction increases. Therefore, α_{v} is replaced by $\alpha_{\mathrm{nuc}}(1-\alpha_{\mathrm{v}})$ for the vaporization

$$m^{+} = C_{\mathrm{vap}} \frac{3\alpha_{\mathrm{nuc}}(1-\alpha_{\mathrm{v}})\rho_{\mathrm{v}}}{R_{\mathrm{B}}} \sqrt{\frac{2}{3} \frac{\max(p_{\mathrm{v}} - p, 0)}{\rho_{\mathrm{l}}}} \tag{8}$$

where $\alpha_{\mathrm{nuc}} = 5 \times 10^{-4}$ is the volume fraction at the nucleation sites and $C_{\mathrm{vap}} = 50$ is an empirical constant for the vaporization.

2.2 *Governing equations and the LES approach*

In the mixture model adopted in this study, the multiphase components share the same velocity and pressure, and the conservation equations of the mass and the momentum are

$$\frac{\partial \rho}{\partial t} + \frac{\partial(\rho u_{\mathrm{j}})}{\partial x_{\mathrm{j}}} = 0 \tag{9}$$

$$\frac{\partial(\rho u_{\mathrm{i}})}{\partial t} + \frac{\partial(\rho u_{\mathrm{i}} u_{\mathrm{j}})}{\partial x_{\mathrm{j}}} = -\frac{\partial p}{\partial x_{\mathrm{i}}} + \frac{\partial}{\partial x_{\mathrm{j}}}\left(\mu \frac{\partial u_{\mathrm{i}}}{\partial x_{\mathrm{j}}}\right) \tag{10}$$

where u_{i} is the velocity component in the i direction, p is the mixture pressure, μ is the laminar viscosity and ρ is the mixture density,

$$\mu = \alpha_{\mathrm{v}}\mu_{\mathrm{v}} + (1-\alpha_{\mathrm{v}})\mu_{\mathrm{l}} \tag{11}$$

$$\rho = \alpha_{\mathrm{v}}\rho_{\mathrm{v}} + (1-\alpha_{\mathrm{v}})\rho_{\mathrm{l}} \tag{12}$$

where α is the volume fraction of one component, and the subscripts l and v represent the liquid and vapor phases, respectively.

The LES equations are derived by applying a Favre-filtering operation to Eqs. (1) and (2)

$$\frac{\partial \rho}{\partial t} + \frac{\partial(\rho \bar{u}_{\mathrm{j}})}{\partial x_{\mathrm{j}}} = 0 \tag{13}$$

$$\frac{\partial(\rho \bar{u}_{\mathrm{i}})}{\partial t} + \frac{\partial(\rho \bar{u}_{\mathrm{i}} \bar{u}_{\mathrm{j}})}{\partial x_{\mathrm{j}}} = -\frac{\partial \bar{p}}{\partial x_{\mathrm{i}}} + \frac{\partial}{\partial x_{\mathrm{j}}}\left(\mu \frac{\partial \bar{u}_{\mathrm{i}}}{\partial x_{\mathrm{j}}}\right) - \frac{\partial \tau_{\mathrm{ij}}}{\partial x_{\mathrm{j}}} \tag{14}$$

where the over-bars denote the filtered quantities, and τ_{ij} arethe SGS stresses, as the unknowns

$$\tau_{\mathrm{ij}} = \rho(\overline{u_{\mathrm{i}} u_{\mathrm{j}}} - \overline{u_{\mathrm{i}}}\,\overline{u_{\mathrm{j}}}) \tag{15}$$

A commonly used way to close the SGS stresses is based on the eddy-viscosity model hypothesis

$$\tau_{\mathrm{ij}} = -2\mu_{\mathrm{t}}\bar{S}_{\mathrm{ij}} \tag{16}$$

where μ_{t} is the eddy viscosity, $\bar{S}_{\mathrm{ij}}$ is the rate-of-strain tensor for the resolved scale

$$\bar{S}_{\mathrm{ij}} = \frac{1}{2}\left(\frac{\partial \bar{u}_{\mathrm{i}}}{\partial x_{\mathrm{j}}} + \frac{\partial \bar{u}_{\mathrm{j}}}{\partial x_{\mathrm{i}}}\right) \tag{17}$$

The present paper adopts the wall-adapting local eddy-viscosity (WALE) model to compute the eddy viscosity, which is modeled as

$$\mu_{\mathrm{t}} = \rho L_{\mathrm{S}}^{2} \frac{(S_{\mathrm{ij}}^{\mathrm{d}} S_{\mathrm{ij}}^{\mathrm{d}})^{3/2}}{(\bar{S}_{\mathrm{ij}}\bar{S}_{\mathrm{ij}})^{5/2} + (S_{\mathrm{ij}}^{\mathrm{d}} S_{\mathrm{ij}}^{\mathrm{d}})^{5/4}} \tag{18}$$

where L_{S} and $S_{\mathrm{ij}}^{\mathrm{d}}$ in the WALE model are expressed as

$$L_{\mathrm{S}} = \min(\kappa d, C_{\mathrm{w}} V^{1/3}) \tag{19}$$

$$S_{\mathrm{ij}}^{\mathrm{d}} = \frac{1}{2}(\bar{g}_{\mathrm{ij}}^{2} + \bar{g}_{\mathrm{ji}}^{2}) - \frac{1}{3}\delta_{\mathrm{ij}}\bar{g}_{\mathrm{kk}}^{2}\,,,\quad \bar{g}_{\mathrm{ij}} = \frac{\partial \bar{u}_{\mathrm{i}}}{\partial x_{\mathrm{j}}} \tag{20}$$

where κ is von Karman's constant, d is the distance to the closest wall, V is the volume of the computational cell and C_{w} is the default WALE constant with a value of 0.5. The WALE model can yield a zero turbulence viscosity for laminar shear flows and has performed well in many cases.

2.3 *Simulation setup*

2.3.1 Computational domain and boundary setup

The flow inside a jet pump can be simplified to a confined axial symmetric flow. Figure 4 shows the computational domain used in this study. To simulate the flow in a jet pump, the outlet pipe and the suction pipe have generally an enough length to ensure that the flows at the inlet and the outlet are stable and fully developed. The domain inlet is $8D_{\text{in}}$ upstream the suction chamber, and the outlet is $8D_{\text{out}}$ downstream the diffuser. The boundary conditions of the inlet of the primary flow and the secondary flow are set as the velocity inlet. The outlet is fixed at the static pressure, and all other surfaces are imposed as non-slip walls. The computational fluid dynamics (CFD) code ANSYS-CFX is used for the simulations.

2.3.2 Mesh information

To strikea balance between the computational cost and the calculation accuracy, three sets of meshes with coarse, medium, and fine resolutions are generated based on the same topology with a constant refinement ratio $\sqrt{2}$. The y plus value is about 1 in all three meshes. The medium grid, shown in Fig. 5, contains 4 108 432 cells. The mesh from the suction chamber to the diffuser is refined to capture the highly turbulent flow structure.

2.3.3 Calculation setup

The time-dependent governing equations are discretized in both space and time with the direct pressure-velocity coupling method to solve the equations. The higher order scheme is used for the convection terms. The second order backward Euler algorithm is used for the time integration. Thirty iterations per time step are used to balance the accuracy and the efficiency. The convergence criterion involves the root mean square (RMS) residual target of 5×10^{-5}, which is sufficient for unsteady flows with cavitation. The cavitation simulations are carried out with the steady results as the values in the initial conditions. Then, the cavitation model and the unsteady solver are used for the cavitation flow simulation. In the present case, we select a time step $\Delta t = 1\times10^{-5}$ s to carry out the unsteady cavitating flow simulations in the jet pump, in view of the computation's use of resources.

3. Results and discussions

3.1 *Comparison of the fundamental performance between experiments and simulations*

The fundamental performance of a jet pump can be characterized by the dimensionless performance parameters such as the flow rate ratio (q), the pressure ratio (h) and the efficiency (η). The expression of q, h and η can be defined as follows:

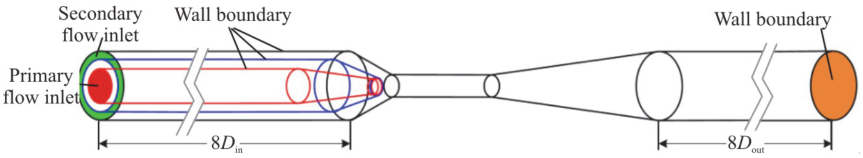

Fig. 4 (Color online) Computational domain and boundary condition

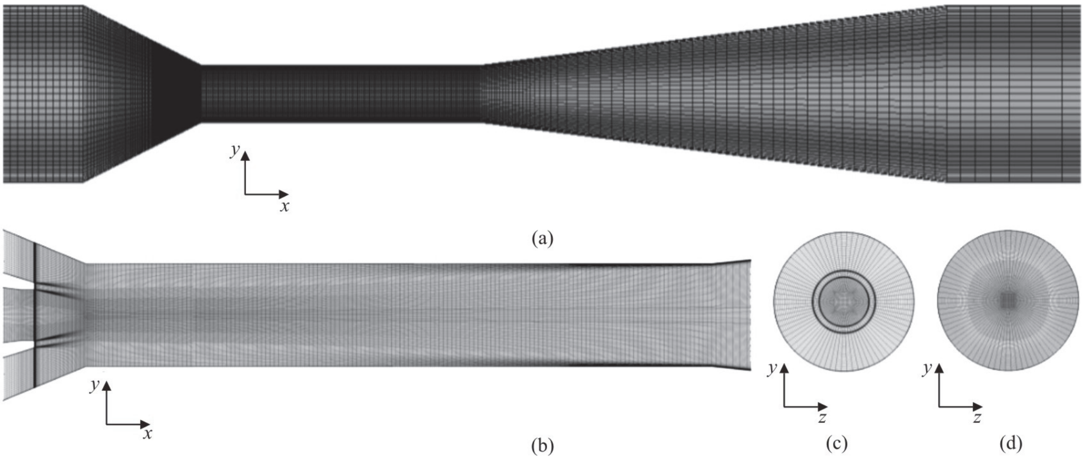

Fig. 5 Computational grid of the computational domain: (a) x-y view, (b) x-y view in the z symmetry plane of the throat region, (c) y-z view in the nozzle exit cross section, (d) y-z view in the throat cross section

$$q = \frac{Q_{\mathrm{s}}}{Q_{\mathrm{in}}} \tag{21}$$

$$h = \frac{P_{\mathrm{out}} - P_{\mathrm{s}}}{P_{\mathrm{in}} - P_{\mathrm{s}}} = -\frac{\left(\dfrac{p_{\mathrm{out}}}{\rho_{\mathrm{out}} g} + \dfrac{v_{\mathrm{out}}^2}{2g} + z_{\mathrm{out}}\right) - \left(\dfrac{p_{\mathrm{s}}}{\rho_{\mathrm{s}} g} + \dfrac{v_{\mathrm{s}}^2}{2g} + z_{\mathrm{s}}\right)}{\left(\dfrac{p_{\mathrm{in}}}{\rho_{\mathrm{in}} g} + \dfrac{v_{\mathrm{in}}^2}{2g} + z_{\mathrm{in}}\right) - \left(\dfrac{p_{\mathrm{s}}}{\rho_{\mathrm{s}} g} + \dfrac{v_{\mathrm{s}}^2}{2g} + z_{\mathrm{s}}\right)} \tag{22}$$

$$\eta = \frac{Q_{\mathrm{s}}(P_{\mathrm{out}} - P_{\mathrm{s}})}{Q_{\mathrm{in}}(P_{\mathrm{in}} - P_{\mathrm{out}})} = q\frac{h}{1-h} \tag{23}$$

where Q is the volume flow rate, P_{out} and P_{in} are the total pressure in the outlet and the inlet, p is the static pressure, g is the acceleration of gravity, v is the cross-sectional average velocity and z is the elevation. The subscripts in, out and s represent the inlet of the primary flow, the outlet of the diffuser and the suction pipe, respectively.

Table 3 summarizes the experimental conditions of the unstable limitedoperation stage selected for this study.

Table 3 Experimental conditions of unstable limited operation stage

p_{in} /kPa	p_{out} /kPa	q	h
400	195.856	0.413	0.354

Table 4 presents the experimental data and the calculated results of the pressure ratio (h) and the efficiency (η). δ_h and δ_η are the relative errors between the experimental and numerical results for h and η, respectively. Firstly, with the increase of the flow rate ratio q, the pressure ratio h decreases gradually, and the efficiency η increases to a maximum value and then decreases gradually. However, when the flow rate ratio q increases to a certain value, it will no longer increase and then stay in a stable value. At this point, the cavitation in the jet pump becomes very turbulent and unstable with significantly drop of the pressure ratio h and the efficiency η. The results for the unsteady cavitation flow in Table 4 show that the numerical results in the three cases agree well with the experimental data, which means that the numerical methods adopted in this paper are appropriate to simulate the cavitating flow in a jet pump. Moreover, the difference between the middle and fine resolution meshes is very small for h and η. Hence, the middle resolution mesh is used as the final grid. The numerical results presented in the following are all for the case with the middle resolution mesh, the case 2.

Table 4 Results of the mesh number independence test

	Mesh number	h	δ_h /%	η	δ_η /%
Case 1	1 400 470	0.336	–5.085	0.209	–7.522
Case 2	4 108 432	0.357	0.847	0.229	1.327
Case 3	11 609 580	0.356	0.565	0.227	0.442
Exp.	-	0.354	-	0.226	-

To further validate the numerical methods, the numerical results of the pressure coefficient are compared with the experimental data. Figure 6 shows the experimental and numerical pressure coefficient distributions along the jet pump wall. The pressure coefficient is defined as

$$C_{\mathrm{p}} = \frac{p - p_{\mathrm{s}}}{\dfrac{1}{2}\rho_{\mathrm{l}} v_{\mathrm{n}}^2} \tag{24}$$

where p_{s} is the static pressure of the secondary flow, p is the static pressure at any point on the jet pump wall and v_{n} is the cross-sectional mean velocity at the nozzle exit.

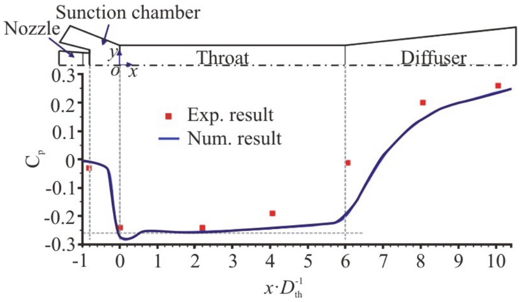

Fig. 6 (Color online) Comparison of the measured and predicted pressure coefficient distribution

The y-axis and the x-axis in Fig. 6 denote the pressure coefficient and the normalized distance from the jet pump nozzle, respectively, to show the experimental and numerical time-average pressure coefficient distributions along the jet pump wall. From Fig. 6, the predicted pressure distribution obtained by the LES methods is in good agreement with the experiment results. The pressure decreases sharply with the primary flow and the secondary flow mixing at the suction chamber. The minimum pressure appears around the junction of the suction chamber and the throat. The pressure stays almost unchanged upstream the throat, but starts to increase when the mixed flow goes toward the throat downstream. The place where the pressure rises in the simulations agrees well with the experimental results, and it is also the case for the place where the cavitation cloud collapses. When the mixed flow goes into the diffuser, the pressure rises significantly, and it will increase to its maximum, as will the outlet pressure.

Some differences can be seen between the simulated C_p distributions and the experimental results, especially the rate of the pressure increase in the throat. It is observed that the pressure in the cavity trailing rises rapidly according to the experimental measurements, while according to the numerical results a much slower rising is observed. The cloud cavitation sheds and collapses rapidly at the junction of the throat and the diffuser. The great effect of the cavitation collapsing on the local pressure rising can be rightly reproduced by experiments. However, the incompressible treatment and the adopted cavitation model can not fully capture the effect of the dramatic and turbulent cloud cavitation collapsing, so the tendency of the pressure rising is much reduced as compared to the experiments. Nevertheless, the main tendency of the C_p distributions is reasonably reproduced by the numerical results, especially the region of the pressure rebound is the same as in the experimental results.

3.2 *Comparison of the evolution of cavitation over-time between experiments and simulations*

To illustrate the transient cavitation behavior of the unsteady cavitating flow in a jet pump, the total vapor volume V_{cav} is calculated at each time step as shown in Fig. 7, with a time step of 5×10^4 in the unsteady calculations, where V_{cav} is defined as

$$V_{\mathrm{cav}} = \sum_{\mathrm{i}=1}^{N} \alpha_{\mathrm{i}} V_{\mathrm{i}} \tag{25}$$

where N is the total number of control volumes in the computational domain, α_{i} is the vapor volume fraction in each control volume and V_{i} is the volume of each cell.

As shown in Fig. 7, the total cavity volume shows clearly quasi-periodic behaviors over time, with the cavity growing and collapsing. Figure 8 shows the numerical total cavity volume variation over two typical cycles to better illustrate the evolution of the predicted turbulent cavitating flow over time.

A series of snapshots during one cycle period (T_{cycle} in Fig. 8) shows the evolution of the unsteady cavitation in the throat over time. Figure 9 shows seven experimental and numerical snapshots, which demonstrate the three-dimensional structures of the experimental and numerical cavitation results. The cavitation is represented by the vapor volume fraction value of 0.1. Figure 9(c) is the pressure distribution in the throat of the jet pump.

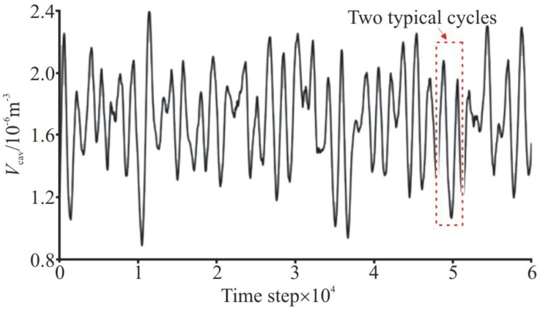

Fig. 7 (Color online) Variation of the cavity volume

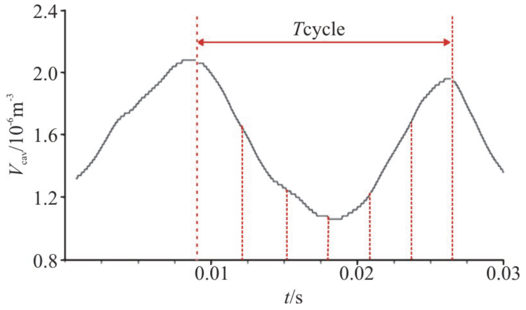

Fig. 8 (Color online) One typical cycle

At the unstable limited operation stage in Fig. 9, the flow begins to accelerate, with a pressure drop due to the reduced sectional area in the jet pump. The inception of the cavitation first occurs at the junction of the suction chamber and the throat, with a decreased pressure. This can also lead to the cavity boosting growing here. The drastically oscillating cavity cloud, with its highly unstable features, appears in the throat, and then it develops downstream the throat. Finally, the cavity cloud collapses and its length decreases due to the increase of the pass area and the local high pressure in the diffuser, as shown in Fig. 9(c). In the shear cavitation, the instability of the cavitation depends on the expansion. characteristics of the streamwise or spanwise vortices.

The typical cycle in Fig. 9 involves the process of contraction and regrowth of the cavitation cloud in the jet pump. At $t = T_0$ in Fig. 9, the cavity cloud is collapsed at the downstream of the throat and it can

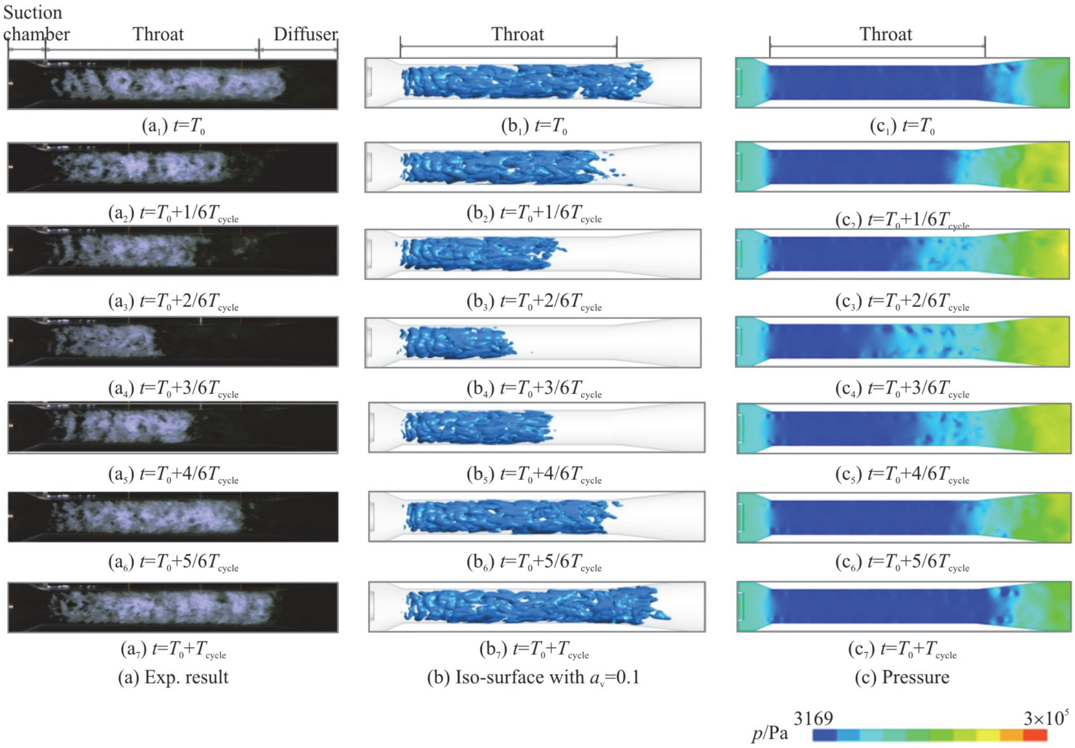

(a$_1$) t=T_0 (b$_1$) t=T_0 (c$_1$) t=T_0

(a$_2$) t=T_0+1/6T_{cycle} (b$_2$) t=T_0+1/6T_{cycle} (c$_2$) t=T_0+1/6T_{cycle}

(a$_3$) t=T_0+2/6T_{cycle} (b$_3$) t=T_0+2/6T_{cycle} (c$_3$) t=T_0+2/6T_{cycle}

(a$_4$) t=T_0+3/6T_{cycle} (b$_4$) t=T_0+3/6T_{cycle} (c$_4$) t=T_0+3/6T_{cycle}

(a$_5$) t=T_0+4/6T_{cycle} (b$_5$) t=T_0+4/6T_{cycle} (c$_5$) t=T_0+4/6T_{cycle}

(a$_6$) t=T_0+5/6T_{cycle} (b$_6$) t=T_0+5/6T_{cycle} (c$_6$) t=T_0+5/6T_{cycle}

(a$_7$) t=T_0+T_{cycle} (b$_7$) t=T_0+T_{cycle} (c$_7$) t=T_0+T_{cycle}

(a) Exp. result (b) Iso-surface with a_v=0.1 (c) Pressure

Fig. 9 (Color online) Time evolution of cavitation in jet pump within one typical cycle

not continue to expand to the diffuser. From $t = T_0 + 1/6T_{\text{cycle}}$ to $t = T_0 + 3/6T_{\text{cycle}}$, the cavitation length is seen to decrease gradually in the throat, but the cloud cavity structure in the throat front section remains almost unchanged. As shown in Fig. 9(c), the local high pressure develops from the diffuser to the place near the middle of the throat, leading to the cavity collapse from $t = T_0 + 1/6T_{\text{cycle}}$ to $t = T_0 + 3/6T_{\text{cycle}}$. From $t = T_0 + 3/6T_{\text{cycle}}$ to $t = T_0 + 5/6T_{\text{cycle}}$, the cloud cavitation grows again due to the local pressure decrease at the downstream of the throat, with the boundary of the cavitation cloud collapsing moving downstream. Finally, at $t = T_0 + T_{\text{cycle}}$, with the boundary of the cavitation cloud collapsing and reaching the tail of the throat, the condition shown in $t = T_0$ is restored. At this point, the cavitation cloud completes a whole contraction and regrowth process, and then the process will be repeated. The comparison between the experimental results and the predicted cavitation patterns in Fig. 9 shows that the LES results can accurately capture the feature of the cavitation time evolution, in a good agreement with the experiments.

3.3 *Evolution of cavitation and vortex structure over time*

3.3.1 Inception of annular vortex cavitation

In the jet pump, one sees a typical turbulent shear flow. The inception and the development of the cavitation in shear flows are usually controlled by the local vortex structure. Kelvin Helmholtzin stability is found in a jet pump, similar to that in a free shear flow. This instability can lead to a periodic shedding of the annular vortex structure downstream the nozzle. When the annular vortex structure is transported into the throat, the annular vortex cavitation occurs due to the local low pressure in the throat.

Figure 10 presents the detailed growth process of the typical annular vortex cavitation in a jet pump. Figures 10(a) and 10(b) are the experimental and numerical results, respectively. The pictures from $t = 0$ ms to $t = 0.15$ ms are at the same location within the monitored window. In Fig.10(a), at $t = 0$ ms, the local pressure becomes concentrated in the throat, and a few bubbles appear due to the Kelvin Helmholtz instability existing with a high shear effect in the throat, marked by the white arrows 1, 2 and 3. Figure 10(b) shows the same phenomenon, marked by the red arrows 1 and 2. These bubbles begin to grow and integrate mutually when the main flow transports them toward the downstream side of the throat. Finally, in Fig. 10 at $t = 0.15$ ms, a full annular vortex cavitation is formed, as shown by the white arrow 4 and the red arrow 3. The cores of the vortices are at the locations of pressure drops, as the potential sites of the cavitation. When the annular vortex is strong enough and the pressure in the vortex core is low enough, the annular vortex cavitation is induced.

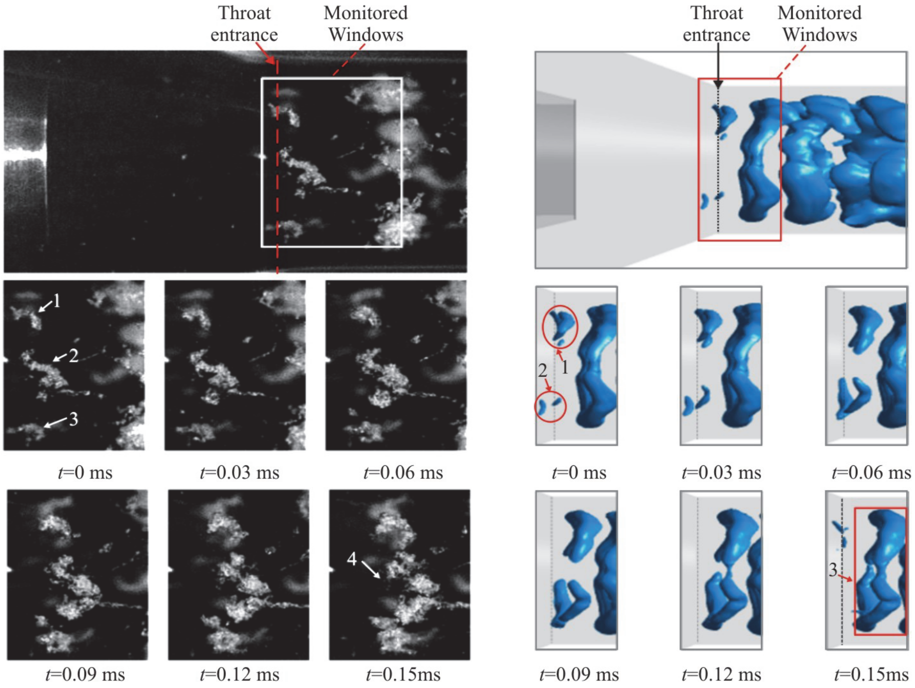

(a) Exp. result (b) Iso-surface with $a_v=0.1$

Fig. 10 (Color online) Growth process of one typical annular vortex cavitation

3.3.2 Development and merging of annular vortex cavitation

To analyze the cavitation and vortex structure development in detail, Fig. 11 presents the cavitation and vortex development within 1 ms. In experimental photos, it is difficult to distinguish the detailed annular vortex cavitation development due to the limited resolution. The analysis of the annular vortex cavitation development is therefore mainly based on the numerical results. Figure 11(a) shows the cavitation structure with an iso-surface of $\alpha_v = 0.1$, and Fig. 11(b) shows the vortex structure visualized by the Q-criterion.The Q-criterion is a promising criterion of coherent structures that can be used to visualize the structures of turbulent flows. It is defined as

$$Q = \frac{1}{2}(\|\Omega\|^2 - \|S\|^2) \tag{26}$$

where Ω is the vorticity tensor, S is the rate of the strain tensor.

The value taken in the Q-criterion is $3\times10^6\ \mathrm{s}^{-2}$, colored with the streamwise velocity. The vortex structure is complicated, and the development of the cavitation is irregular, as shown in Fig. 11. Figure 11(b) shows the vortex rings upstream the throat, corresponding to the annular vortex cavitation shown in Fig.11(a).

The annular vortex cavitation is transported downstream because the transport of the main flow plays the dominant role in a jet pump. Moreover, some of the annular vortex cavitation is merged or broken during this process. As shown in Fig. 11(a) from $(1\text{-}t_3)$ to $(1\text{-}t_6)$, there is a ribbed vortex cavitation between the two annular vortex cavitations, connecting the front and back annular vortex cavitations. This connection clearly shows the dynamic development of the annular vortex cavitation. With the development of the cavitation as shown in Fig. 11(a) from $(2\text{-}t_1)$ to $(2\text{-}t_3)$, the annular vortex cavitation gradually breaks due to the stretching of the ribbed vortex. Another different phenomenon can be observed in Fig. 11(a) from $(3\text{-}t_1)$ to $(3\text{-}t_6)$. A single bubble appears in the throat, and this small bubble gradually grows and finally joins together with the surrounding, large cloud cavitation.

The process of the development, the merging and the breaking of the annular vortex cavitation is closely related to the local vortex structure. Further exploration into the coherent structures formed in the jet pump might be necessary for a better understanding of the cavitation. The flow in the jet pump is a confined coaxial jet, which is quite different from the free shear flow. The vortex at the downstream of the jet pump will not develop into a planar vortex ring. In a high Reynolds number flow, the vortex rings are very instable and their shapes are easily changed when

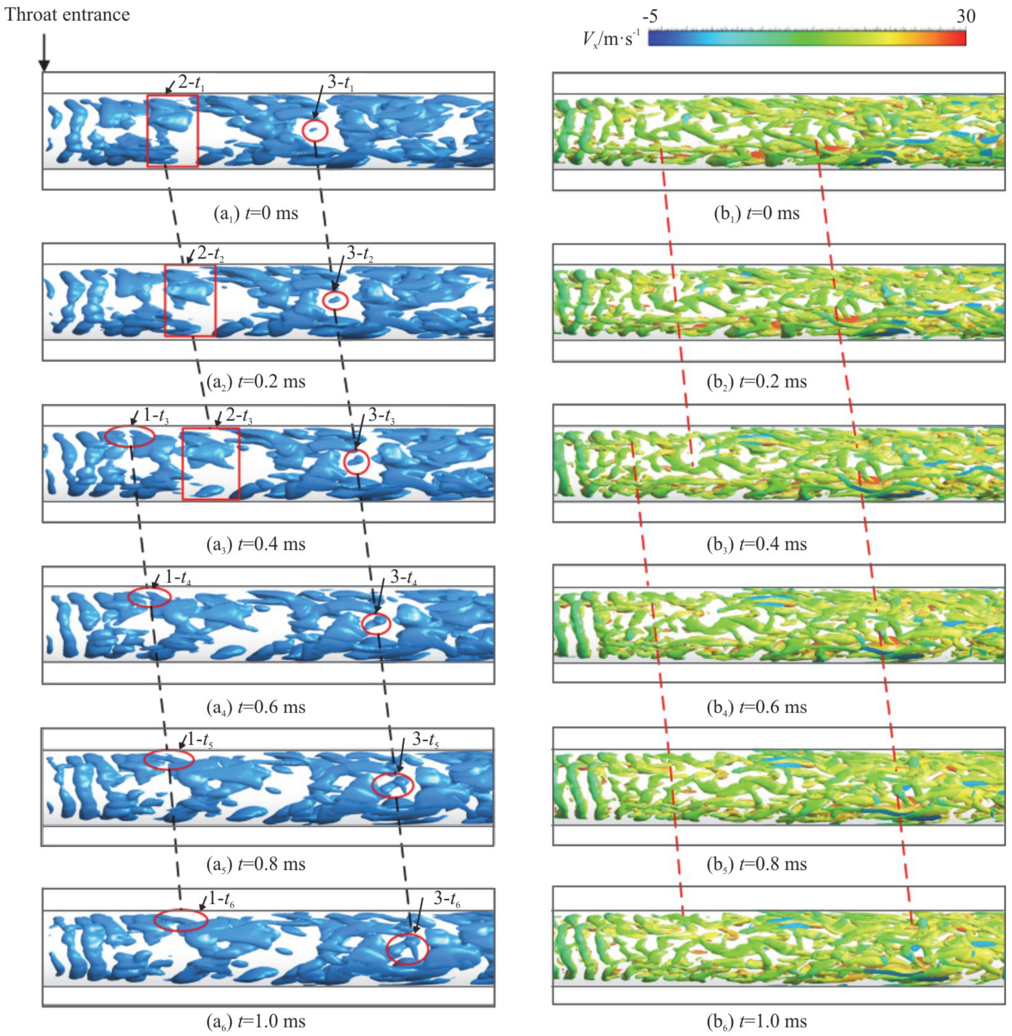

(a) Iso-surface with a_v=0.1

(b) Iso-surface of Q-criterion (Q=3×10^6 s^{-2})

Fig. 11 (Color online) The predicted vortex evolution in jet pump with iso-surface of $\alpha_v = 0.1$ and $Q = 3\times10^6\ \mathrm{s}^{-2}$

they are disturbed. Figure 12 presents the process of the annular vortex cavitation merging. The annular vortex becomes to assume a jagged shape due to the instability of the vortex rings. As seen from the red frame shown in Fig. 12, when the local pressure decreases and the jagged shape vortex develops, the local cavity bubbles appear to promote the merging of the annular vortex cavitation. In Fig. 13, the annular vortex recorded by experiments is pointed by the yellow arrows. The merging process of the front and back annular vortices takes place with a high pairing instability, leading to the complicated streamwise and spanwise ribbed vortices. Then the annular vortex cavitation develops according to the change of the vortex structure. As the red arrow points out in Fig. 13, there is streamwise filiform vortex cavitation appearing during the process of the merging of the annular vortex cavitation.

The process of the development, the merging and the breaking of the annular vortex cavitation is closely related to the local vortex structure. Further exploration into the coherent structures formed in the jet pump might be necessary for a better understanding of the cavitation. The flow in the jet pump is a confined coaxial jet, which is quite different from the free shear flow. The vortex at the downstream of the jet pump will not develop into a planar vortex ring. In a high Reynolds number flow, the vortex rings are very instable and their shapes are easily changed when they are disturbed. Figure 12 presents the process of the annular vortex cavitation merging. The annular vortex becomes to assume a jagged shape due to the instability of the vortex rings. As seen from the red frame shown in Fig. 12, when the local pressure decreases and the jagged shape vortex develops, the local cavity bubbles appear to promote the merging of the annular vortex cavitation. In Fig. 13, the annular vortex recorded by experiments is pointed by the yellow arrows. The merging process of the front and back annular vortices takes place with

a high pairing instability, leading to the complicated streamwise and spanwise ribbed vortices. Then the annular vortex cavitation develops according to the change of the vortex structure. As the red arrow points out in Fig. 13, there is streamwise filiform vortex cavitation appearing during the process of the merging of the annular vortex cavitation.

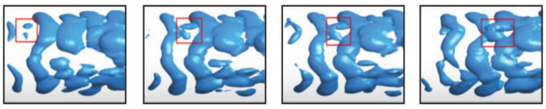

(a) Iso-surface with $a_v=0.1$

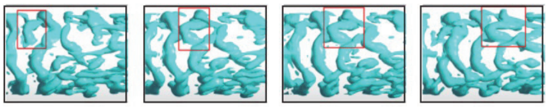

(b) Iso-surface with $Q=3\times10^6\ \mathrm{s}^{-2}$

Fig. 12 (Color online) The process of the merging of annular vortex cavitations

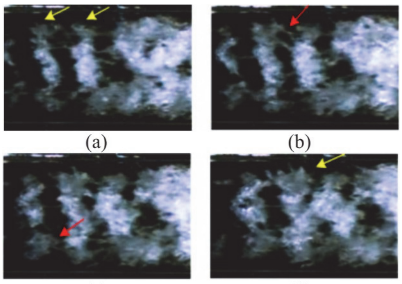

(a) (b)

(c) (d)

Fig. 13 (Color online) The sketch of merging process of annular vortices by experimental record

3.3.3 Collapse of the annular vortex cavitation

Figures 14(a) and 14(b) show the typical collapse of the cavitation at the tail of the throat obtained from the experimental observations and the numerical predictions, respectively. Figure 14(c) is the vortex structure shown by iso-surface of the Q-criterion. At the end of the throat where the cavitation collapses, the vortex structure becomes complicated, and it is hard to identify the vortex structure clearly. The vortex shape based on the Q-criterion is much more complicated than that based on the vapor volume fraction. The cloud cavitation collapses downstream the throat, but the vortex can still develop into the diffuser. Unlike the illustrations in Sections 3.3.1 and 3.3.2, the interaction between the vortices and the viscous effect is the main factor leading to the process of the large vortex structure continually breaking into smaller vortices.

The well-known re-entrant jet mechanism has been verified as a significant cause of the unsteadiness of the cavitating flow. Due to the adverse pressure gradient at the downstream, the flow at the downstream goes towards the upstream and moves into the cavitation area. Finally, this flow cuts off the continuous cavitation region, resulting in the cavitation in stability. The cloud cavitation will collapse in a jet pump due to the local high pressure downstream the throat. This process is related to the influence of the re-entrant jet. Figure 14 shows the re-entrant jet visualized and highlighted by the velocity vector. The cavity seems to be squeezed and pushed downstream by the combination of the re-entrant jet and the ambient main flow. With the pressure rising downstream, the vapor cloud finally collapses, with few bubbles surviving at the exit of the diffuser.

3.4 *Cavitation-vortex interaction*

The complicated cavitation flow is closely related to the vortex, as mentioned above. Therefore, the vorticity transport equation is used to investigate the interaction between the cavitation and the vortex. The vorticity transport equation for the incompressible flow can be written as

$$\frac{\partial\boldsymbol{\omega}}{\partial t}=(\boldsymbol{\omega}\cdot\nabla)\boldsymbol{V}-\boldsymbol{\omega}(\nabla\cdot\boldsymbol{V})+\frac{\nabla\rho\times\nabla p}{\rho^2}+\nu\nabla^2\boldsymbol{\omega} \tag{27}$$

The four terms on the right-hand side are the vortex stretching term (the vorticity change caused by the velocity gradient), the vortex dilatation term (the expansion and the contraction of a fluid element), the baroclinic torque term (the vorticity change by the misaligned gradients of the pressure and the density), and the viscous diffusion of the vorticty, from left to right, respectively. The fourth term, the viscous diffusion of the vorticity, can be ignored for the flows with high Reynolds numbers. Then the vorticity transport equation can be simplified as

$$\frac{\mathrm{D}\omega_z}{\mathrm{D}t}=\left[(\omega\cdot\nabla)V\right]_z-\left[\omega(\nabla\cdot V)\right]_z+\left[\frac{\nabla\rho\times\nabla p}{\rho^2}\right]_z \tag{28}$$

$$\omega_z=\frac{\partial V_y}{\partial x}-\frac{\partial V_x}{\partial y} \tag{29}$$

$$[(\omega\cdot\nabla)V]_z=\omega_x\frac{\partial V_z}{\partial x}+\omega_y\frac{\partial V_z}{\partial y}+\omega_z\frac{\partial V_z}{\partial z} \tag{30}$$

$$[\omega(\nabla\cdot V)]_z=\omega_z\left(\frac{\partial V_x}{\partial x}+\frac{\partial V_y}{\partial y}+\frac{\partial V_z}{\partial z}\right) \tag{31}$$

$$\left(\frac{\nabla\rho\times\nabla p}{\rho^2}\right)_z=\frac{1}{\rho^2}\left(\frac{\partial\rho}{\partial x}\frac{\partial p}{\partial y}-\frac{\partial\rho}{\partial y}\frac{\partial p}{\partial x}\right) \tag{32}$$

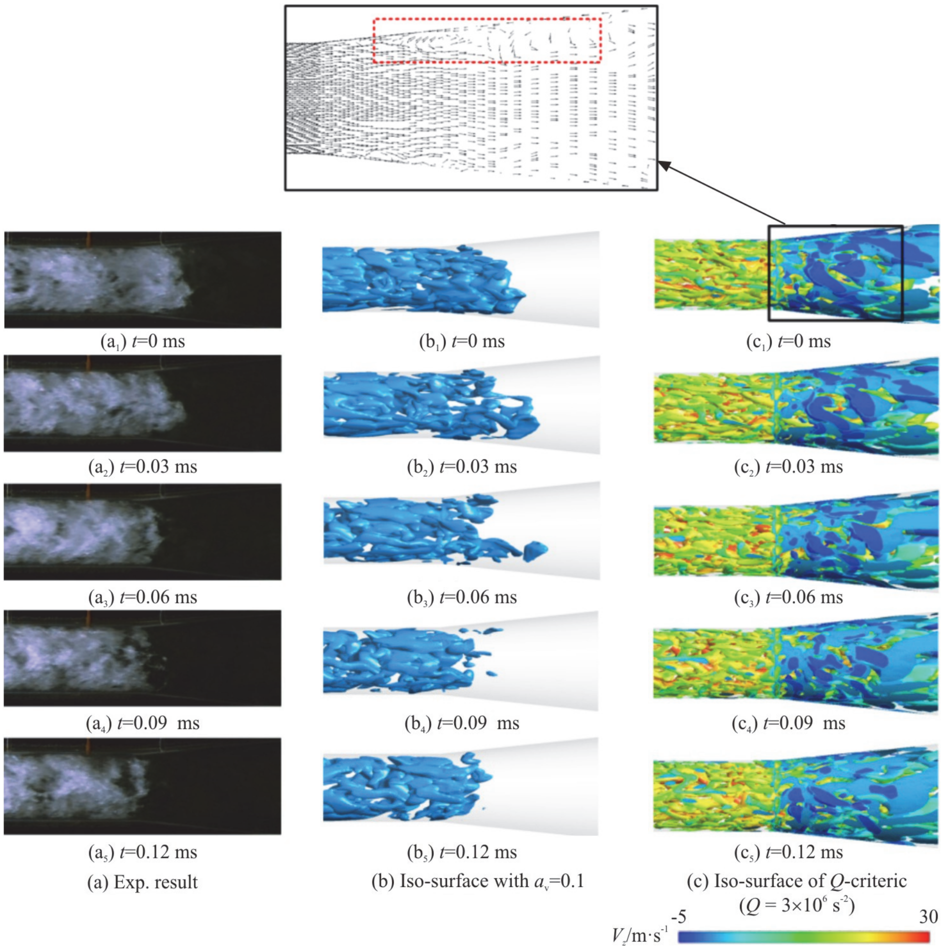

(a_1) t=0 ms (b_1) t=0 ms (c_1) t=0 ms

(a_2) t=0.03 ms (b_2) t=0.03 ms (c_2) t=0.03 ms

(a_3) t=0.06 ms (b_3) t=0.06 ms (c_3) t=0.06 ms

(a_4) t=0.09 ms (b_4) t=0.09 ms (c_4) t=0.09 ms

(a_5) t=0.12 ms (b_5) t=0.12 ms (c_5) t=0.12 ms

(a) Exp. result (b) Iso-surface with a_v=0.1 (c) Iso-surface of Q-criteric ($Q = 3\times10^6$ s^{-2})

Fig. 14 (Color online) The experimental and predicted collapsing of vortex

Figure 15 compares the vapor volume fraction and the vortex stretching, dilatation, and baroclinic torque terms at the mid-plane of a jet pump at a given moment. The jet pump throat is figuratively divided into three sections: the front, the middle, and the end, corresponding to the three processes, that is, the inception of the annular vortex cavitation, the development and the merging of the annular vortex cavitation, and the collapse of the annular vortex cavitation. The distributions of all three terms are closely related to the region in which the cavitation occurs.

At the front of the throat in Fig. 15, the vortex stretching term takes almost the same magnitude as the dilatation term, and both terms are larger than the baroclinic torque term. At the inception, the huge velocity gradient caused by the intersection of the parmary flow and the secondary flow greatly increases the vortex stretching term. The dilatation term is equal to zero in incompressible flows due to the flow continuity. According to this term, the vorticity is increased if the fluid in the vortex region is compressed, and the vorticity is decreased if the fluid undergoes the expansion. The large shear effect also induces a significant phase change, that is, the inception of the annular vortex cavitation. This effect leads to the much larger magnitude of the dilatation term. The vortex stretching and dilatation terms play the main role in the vorticity transport in the inception stage of the annular vortex cavitation. The distribution and the magnitude of the vortex stretching term are clearly smaller at the front of the throat than at the middle and the end. The vorticity is mainly transported by the convection and the diffusion. The vertical velocity gradient is much larger than the streamwise velocity gradient at the inception, and the perturbation from the inflow is selectively enlarged. The streamwise convection transport rate is clearly larger than that of the vertical diffusion, and the shear layer thickness and the vorticity diffusion increase slowly. Due to these factors, the distribution and the magnitude of the vortex stretching term are smaller at the front of the throat than at the middle and the end.

At the middle of the throat as shown in Fig. 15, the dilatation and baroclinic torque terms are much smaller than the vortex stretching term. From the front of the throat to the middle, the magnitude of the vortex stretching increases. With regard to the free shear

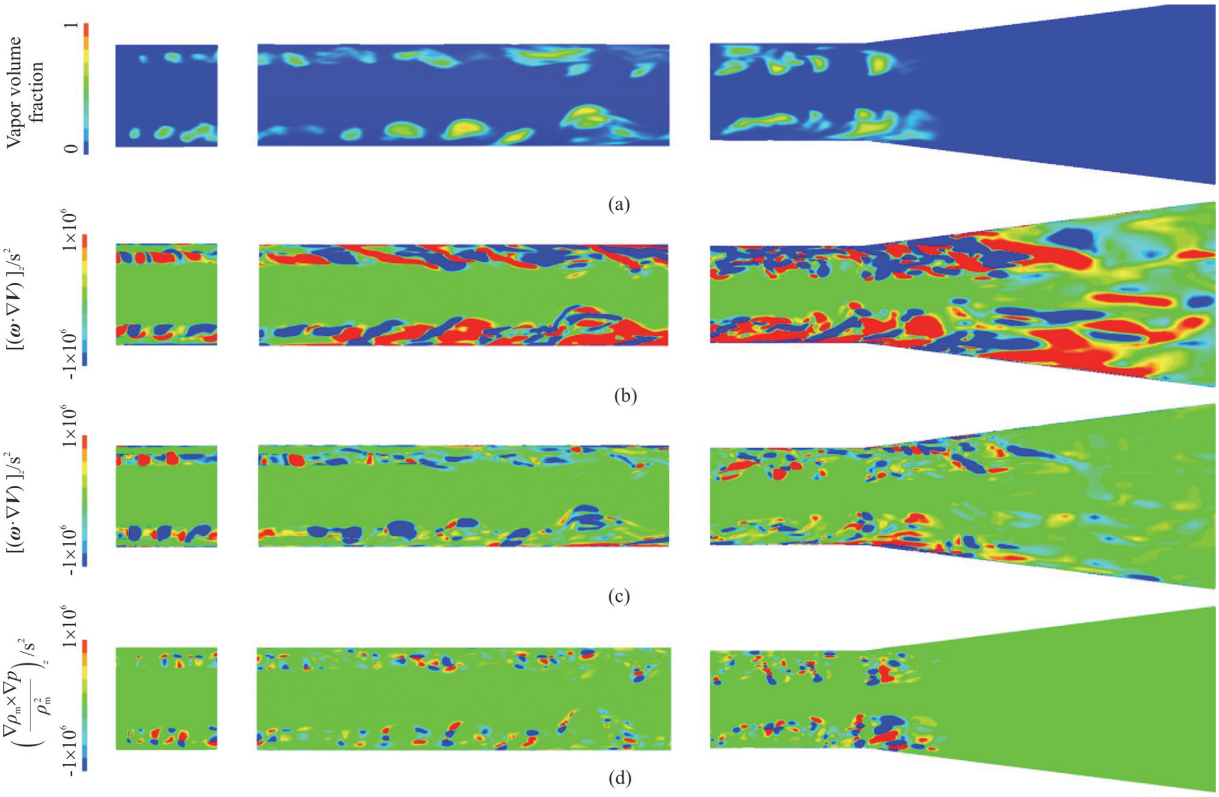

Fig. 15 (Color online) Comparison of the vapor volume fraction, vortex stretching vapor volume fraction, vortex stretching, dilatation and baroclinic torque terms at the mid-plane of jet pump

jet, this process is mainly the pairing and the merging of the vortex[23]. As shown in Figs. 12 and 13, the merging of the annular vortex cavitation happens in this process. Some streamwise filiform vortex cavitation also appears when two annular vortices merge. The merging of the annular vortex cavitation and the generation of the streamwise filiform vortex cavitation both increase the vortex stretching term. As shown in Fig. 15, the distribution and the configuration of the vortex stretching term strongly depends on the cavity evolution. In summary, the process of the merging of the annular vortex cavitation leads to a complicated streamwise vortex and spanwise vortex, which increases the vortex stretching term.

At the end of the throat in Fig. 15, corresponding to the collapse of the annular vortex cavitation, the vortex stretching term remains almost in a same magnitude, while the baroclinic torque term increases along the area of the cloud cavitation collapse. The baroclinic torque term distributes ina few places with a smaller magnitude compared to the vortex stretching term, while the magnitude of the baroclinic torque term increases at the end of the throat compared to those at the front and the middle. The baroclinic torque increases significantly, due to the non-alignment of the density and pressure gradients that results from the collapse of the annular vortex cavitation. Thus, the baroclinic torque is an important source of vorticity during the collapse of the cloud[24-26].

4. Conclusions

The unsteady cavitating flow in a jet pump in the unstable limite doperation stage is investigated both by experiments and numerical simulations. The calculations are based on the LES coupled with the Zwart cavitation model. The experimentally observed cavitating flow features agree well with the numerical results. The influences of the cavitation on the development of the vortex structure and the cavitation-vortex interactions are further investigated based on the vorticity transport equation. The main conclusions are as follows:

(1) Both the experimental and computational results indicate that the evolution of the cavitation in a jet pump over time show sclearly quasi-periodic behaviors, with a cycle of the cavity inception, growth, and collapse in the unstable limited operation stage. In addition, the performance of a jet pump predicted by the LES agrees well with the experimental results. The simulation accurately shows the main tendency of the pressure distribution, especially in the region where the pressure rebounds. This result shows that the LES

results in this paper accurately capture the evolution of the cavitation over time.

(2) The evolution of the vortex structure is closely related to the cavitation. The inception of the annular vortex cavitation might be due to the pressure decreasing in the vortex core when the strength of the annular vortex is increased. The vortex rings in the jet pump are very much unstable, and their shapes change easily when disturbed, which often occurs together with the process of the merging of the annular vortices. The ribbed vortex cavitation can link the front and back annular vortex cavitations within the process of the main flow transport, and this dynamic process usually occurs together with the growth of a great number of small bubbles. As for the cloud cavitation, it will finally collapse in the jet pump due to the local high pressure downstream the throat. This process is often related to the influence of the re-entrant jet.

(3) The cavitation-vortex interaction is investigated based on the vorticity transport equation. At the front of the throat, the vortex stretching term takes a same magnitude as the dilatation term, and these terms play the main role in the vorticity transport in the inception stage of the annular vortex cavitation. At the middle of the throat, the vortex stretching term plays a leading role in the vorticity transport. The vortex stretching term increases during the merging of the annular vortex cavitation and the generation of the cavitation of the streamwise filiform vortices. In addition, the distribution and the configuration of the vortex stretching term strongly depend on the cavity evolution. At the end of the throat, the strength of the baroclinic torque term increases along the area in which the cloud cavitation collapses. The processes of the annular cavitation inception, development, and collapse significantly increase the vortex stretching, dilatation, and baroclinic torque terms.

References

[1] Lu H. Theory and application of injection technolog [M]. Wuhan, China: Wuhan University Press, 2004.

[2] Drozdov A. N. Optimization of flow diagrams of multiphase pump-ejector systems for improving their operational efficiency with combined oil and gas gathering [J]. *Chemical and Petroleum Engineering*, 2014, 50(7-8): 499-503.

[3] Xu M., Ji B., Zou J. et al. Experimental investigation on the transport of different fish species in a jet fish pump [J]. *Aquacultural Engineering*, 2017, 79: 42-48.

[4] Long X., Wang J., Zhang J. et al. Experimental investigation of the cavitation characteristics of jet pump cavitation reactors with special emphasis on negative flow ratios [J]. *Experimental Thermal and Fluid Science*, 2018, 96: 33-42.

[5] Jamaluddin A. R., Ball G. J., Turangan C. K. et al. The collapse of single bubbles and approximation of the far-field acoustic emissions for cavitation induced by shock wave lithotripsy [J]. *Journal of Fluid Mechanics*, 2011, 677: 305-341.

[6] Franc J. P., Michel J. M. Fundamentals of cavitation [J]. *Fluid Mechanics and Its Applications*, 2004, 76(11): 1-46.

[7] Long X., Yao H., Zhao J. Investigation on mechanism of critical cavitating flow in liquid jet pumps under operating limits [J]. *International Journal of Heat and Mass Transfer*, 2009, 52(9): 2415-2420.

[8] Xiao L., Long X. Cavitating flow in annular jet pumps [J]. *International Journal of Multiphase Flow*, 2015, 71: 116-132.

[9] Long Y., Long X. P., Ji B. et al. Verification and validation of URANS simulations of the turbulent cavitating flow around the hydrofoil [J]. *Journal of Hydrodynamics*, 2017, 29(4): 86-96.

[10] Ji B., Long Y., Long X. P. et al. Large eddy simulation of turbulent attached cavitating flow with special emphasis on large scale structures of the hydrofoil wake and turbulence-cavitation interactions [J]. *Journal of Hydrodynamics*, 2017, 29(1): 27-39.

[11] Cheng H. Y., Long X. P., Ji B. et al. 3-D Lagrangian-based investigations of the time-dependent cloud cavitating flows around a Clark-Y hydrofoil with special emphasis on shedding process analysis [J]. *Journal of Hydrodynamics*, 2018, 30(1): 122-130.

[12] Senocak I., Wei S. Interfacial dynamics-based modelling of turbulent cavitating flows, Part-1: Model development and steady-state computations [J]. *International Journal for Numerical Methods in Fluids*, 2004, 44(9): 975-995.

[13] Goncalvès E., Charrière B. Modelling for isothermal cavitation with a four-equation model [J]. *International Journal of Multiphase Flow*, 2014, 59: 54-72.

[14] Zhu J., Rodi W. Computation of axisymmetric confined jets in a diffuser [J]. *International Journal for Numerical Methods in Fluids*, 2010, 14(2): 241-251.

[15] Duke D. J., Schmidt D. P., Neroorkar K. et al. High-resolution large eddy simulations of cavitating gasoline–ethanol blends [J]. *International Journal of Engine Research*, 2013, 14(6): 578-589.

[16] Dittakavi N., Chunekar A., Frankel S. Large eddy simulation of turbulent-cavitation interactions in a venturi nozzle [J]. *Journal of Fluids Engineering*, 2010, 132(12): 121301.

[17] Ji B., Luo X. W., Arndt R. E. A. et al. Large eddy simulation and theoretical investigations of the transient cavitating vortical flow structure around a NACA66 hydrofoil [J]. *International Journal of Multiphase Flow*, 2015, 68: 121-134.

[18] Long X., Cheng H., Ji B. et al. Large eddy simulation and Euler-Lagrangian coupling investigation of the transient cavitating turbulent flow around a twisted hydrofoil [J]. *International Journal of Multiphase Flow*, 2017, 100: 41-56.

[19] Xu M. S., Yang X. L., Long X. P. et al. Numerical investigation of turbulent flow coherent structures in annular jet pumps using the LES method [J]. *Science China Technological Sciences*, 2018, 61(1): 1-12.

[20] Zi H., Zhou L., Meng L. Prediction and analysis of jet pump cavitation using large eddy simulation [J]. *Journal of Physics Conference Series*, 2015, 656: 012142.

[21] Long X., Zhang J., Wang Q. et al. Experimental investigation on the performance of jet pump cavitation reactor at different area ratios [J]. *Experimental Thermal and Fluid Science*, 2016, 78: 309-321.

[22] Zwart P. J., Gerber A. G., Belamri T. A two-phase flow model for predicting cavitation dynamics [C]. *Fifth International Conference on Multiphase Flow*, Yokohama, Japan, 2004, 152.

[23] Samimy M., Webb N., Crawley M. Excitation of free shear-layer instabilities for high-speed flow control [J]. *AIAA Journal*, 2018, 56(5): 1770-1791.

[24] Long Y., Long X., Ji B. et al. Numerical simulations of cavitating turbulent flow around a marine propeller behind the hull with analyses of the vorticity distribution and particle tracks [J]. *Ocean Engineering*, 2019, 189: 106310.

[25] Long Y., Long X., Ji B. et al. Verification and validation of large eddy simulation of attached cavitating flow around a Clark-Y hydrofoil [J]. *International Journal of Multi- phase Flow*, 2019, 115: 93-107.

[26] Wu Q., Huang B., Wang G. et al. The transient characteristics of cloud cavitating flow over a flexible hydrofoil [J]. *International Journal of Multiphase Flow*, 2017, 99: 162-173.